J Eng Math (2009) 63:61–78
DOI 10.1007/s10665-008-9250-2

Applicability of the method of fundamental solutions to 3-D wave–body interaction with fully nonlinear free surface

Nan-Jing Wu · Ting-Kuei Tsay

Received: 1 November 2007 / Accepted: 25 September 2008 / Published online: 23 October 2008

Abstract A numerical model for three-dimensional fully nonlinear free-surface waves is developed by applying a boundary-type meshless approach with a leap-frog time-marching scheme. Adopting Gaussian Radial Basis Functions to fit the free surface, a non-iterative approach to discretize the nonlinear free-surface boundary is formulated. Using the fundamental solutions of the Laplace equation as the solution form of the velocity potential, free-surface wave problems can be solved by collocations at only a few boundary points since the governing equation is automatically satisfied. The accuracy of the present method is verified by comparing the simulated propagation of a solitary wave with an exact solution. The applicability of the present model is illustrated by applying it to the problem of a solitary wave running up on a vertical surface-piercing cylinder and the problem of wave generation in infinite water depth by a submerged moving object.

Keywords Meshless · Method of fundamental solutions · Nonlinear · Water waves · Wave–body interaction

1 Introduction

For several decades, water-wave problems have been studied as potential-flow problems governed by the Laplace equation with nonlinear boundary conditions. Due to the rapidly increasing power of computers, time-dependent three-dimensional wave–body interaction problems can now be simulated numerically. Most of these studies have been carried out with boundary-element methods (BEM), subjected to a mixed Eulerian–Lagrangian (MEL) time-marching approach [1–7]. With MEL, particle trajectories and the nonlinear boundary conditions on the free surface can be predicted via numerical integration in the time domain. The velocity potential of a linear boundary-value problem can then be obtained directly at the next time step. Usually, the prediction of particle trajectories and nonlinear free-surface boundary conditions involve lengthy iteration procedures. The MEL approach is explained in detail in the review paper of Tsai and Yue [8]. As BEM, also called boundary-integral-equation methods (BIEM), are based on solving integral equations, integration along the boundaries is always needed by solving the equations directly. Evaluating these integrals is a tedious task since there are singularities on the boundaries, either fixed or

N.-J. Wu · T.-K. Tsay (✉)
Department of Civil Engineering, National Taiwan University, 1 Roosevelt Rd., Sec. 4, Taipei City, 10617, Taiwan
e-mail: tktsay@ntu.edu.tw

N.-J. Wu
e-mail: d90521005@ntu.edu.tw

moving ones. Meanwhile, the full dense matrices resulting from BEM take a lot of time when solving the linear algebraic system. Although the computation can be speeded up by compressing these full matrices to sparse ones with some approximations such as the fast multipole method, panel clustering or wavelet compression [9–11], the task of computing tedious singular integrals still remains in BEM with some difficulties for implementing free-surface water-wave problems.

Cao et al. [12] proposed that, by moving the singularities away from the boundaries and outside the computational domain, the computational time can be reduced efficiently as a consequence of simplifying the evaluating techniques for the surface integrals. This approach is known as the desingularized boundary-integral-equation method (DBIE). There are two versions of DBIE, namely, direct and indirect methods. The direct version of DBIE still requires boundary-elements/panels/meshes and integration over the panels, but the integration is easier as a result of desingularization. In the indirect approach of DBIE, the integration is carried out on a surface outside the computational domain. By using a one-point quadrature integrating scheme, the integrals can be replaced by the summation of a finite number of singularities (or their derivatives); thus no integration is needed. The approach has been successfully applied to simulate both steady and time-dependent water-wave problems [12–14].

In the last decade, a wide family of methods has emerged that attempt to overcome the requirement of computational grids or meshes. The most common name of this family is meshless methods, while sometimes they are also called mesh-free, grid-free, element-free, mesh-reduction, particle or finite point methods, including Galerkin and collocation methods. All of them share the characteristics of not requiring explicit connectivity information, which includes node-to-node distances, azimuths and the sequential relations among these nodes. The basic idea of meshless methods is the construction of radial basis functions (RBFs) which states only the relationship of node-to-node distances. The RBFs were first developed for interpolation of scattered data [15,16], and later became a kind of artificial neural-network kernels [17]. Applications of solving PDEs with the construction of RBFs have been available for years [18]. Generally speaking, there are two kinds of meshless methods, namely, the domain-type and the boundary-type. In the domain-type meshless method, any single RBF does not satisfy the governing equations, so a large number of collocation points are needed in both the computational domain as well as on the boundaries to obtain a better solution. The advantages are the easy programming and averting the chore of mesh generation since neither the number of nodes nor the matrix size is reduced too much. Many studies towards solving fluid-dynamic problems with domain-type meshless methods exist [19–24]. On the other hand, if there exists some fundamental solution which satisfies the governing equation (such as Laplace, Helmholtz, etc. for example), one can choose fundamental solutions as the radial basis functions and set all the source points (centers of RBFs) outside the computational domain. Then, no singularity will be in the computational domain and only collocation points on the boundary are needed to solve these problems [25,26]. This kind of meshless method also goes by the name of method of fundamental solutions (MFS). The idea of MFS is similar to the indirect DBIE, while the difference is that indirect DBIE still needs some numerical integration along the surface on the boundary or outside the domain, but MFS only employs collocation about the boundary points without needing any mesh generation and numerical integration. Therefore the MFS is more simple and efficient than the DBIE to model nonlinear water-wave problems. It should be noted that the integrals in the indirect DBIE in which the integration is carried out outside the domain can be reduced to the solution form of MFS by using a one-point quadrature integrating scheme.

For simulating fully nonlinear free-surface gravity water-wave problems, Wu et al. [27] proposed a boundary-type meshless method with a leap-frog time-marching scheme which is meshless except on the free surface. Soon, they modified their model into a real meshless one by adopting the interpolating approach of an RBF-type artificial neural network and choose the Gaussian function to be the RBF to fit the free surface [28]. Although theoretically their method could be suitable for three-dimensional wave–body interaction problems, they applied it only to two-dimensional wave cases in a fixed sea-bed region, without any wave–body interaction. Furthermore, the free-surface boundary conditions were estimated slightly off in their numerical approximation, so that the wave crests were a little underestimated. Here, the free-surface boundary conditions are correctly formulated and verified with an exact solitary-wave solution. The applicability of the present meshless method for three-dimensional wave–body interaction problems is demonstrated.

2 Mathematical description

2.1 Governing equation

When a water-wave problem is undertaken as a potential-flow problem, there exists a velocity potential satisfying the Laplace equation

$$\nabla^2\phi = 0, \tag{1}$$

where $\phi(\vec{x}, t)$ is the velocity potential, in which $\vec{x}$ denotes the position vector in three-dimensional space, and $\nabla^2 = \frac{\partial^2}{\partial x^2} + \frac{\partial^2}{\partial y^2} + \frac{\partial^2}{\partial z^2}$ is the Laplacian operator. The velocity vector is defined as $\vec{v} = \nabla\phi$.

2.2 Boundary conditions

At the free surface the boundary conditions are specified as follows

$$\frac{\partial\phi}{\partial z} = \frac{\partial\eta}{\partial t} + \nabla_h\phi \cdot \nabla_h\eta, \tag{2}$$

$$\frac{\partial\phi}{\partial t} = -g\eta - \frac{1}{2}\nabla\phi \cdot \nabla\phi + C(t), \tag{3}$$

where $\eta(x, y, t)$ is the free-surface displacement and $\nabla = \frac{\partial}{\partial x}\vec{i} + \frac{\partial}{\partial y}\vec{j} + \frac{\partial}{\partial z}\vec{k}$ is a three-dimensional operator while $\nabla_h = \frac{\partial}{\partial x}\vec{i} + \frac{\partial}{\partial y}\vec{j}$ is a horizontal (two-dimensional) operator. The integral constant $C(t)$ can be set to zero if the water is initially still. The above two equations are called the kinematic and dynamic free-surface boundary conditions (K.F.S.B.C and D.F.S.B.C), respectively.

Beneath the free surface, the no-flux boundary condition is applied at a solid boundary surface, that is,

$$\nabla\phi \cdot \vec{n} = \vec{v}_b \cdot \vec{n} \tag{4}$$

where $\vec{n}$ is the normal vector pointing outward from the body surface and $\vec{v}_b$ is the velocity of the body surface.

2.3 Initial condition

In wave problems with initially still water, the initial condition can be set as

$$\phi(\vec{x}, 0) = 0. \tag{5}$$

For other cases in which the water is not initially still, the initial condition should be given as known. As the governing equation and the boundary conditions and initial conditions are given, the problems of wave motion are well posed and can be solved numerically.

3 Numerical implementation

3.1 Radial basis functions

Firstly, the time domain is discretized by using the symbol the (n) to denote the n-th time step. Based on the concept of meshless methods, the numerical solution of the velocity potential is assumed to be a linear combination of N radial basis functions. Thus

$$\phi^{(n)}(\vec{x}) = \sum_{i=1}^{N} \alpha_i^{(n)} p_i^{(n)}(\vec{x}), \tag{6}$$

where $p_i^{(n)}(\vec{x})$ is the radial basis function (RBF) whose origin (also named source point) is at $\vec{x}_i^{(n)}$ at the instant of the n-th time step with $\alpha_i^{(n)}$ as its weight factor. The type of RBF chosen for ϕ in this study is the fundamental solution of a 3-D Laplacian operator, that is,

$$p_i^{(n)}(\vec{x}) = 1/r_i^{(n)}(\vec{x}), \tag{7}$$

where $r_i^{(n)}(\vec{x}) = \left|\vec{x} - \vec{x}_i^{(n)}\right|$ is the distance from any position in the computational domain to that specific source point. The solution form satisfies the governing equation automatically throughout the computational domain, even if all the RBF centers are chosen outside the computational domain. The solution at each time step can then be obtained by solving $\alpha_i^{(n)}$ from the matrix collocated from the boundary conditions only. At each time step there are N unknowns ($\alpha_i^{(n)},\ i = 1, \ldots, N$) to be solved. Thus, N boundary points are needed for the method of collocation. Based on the solution form in Eq. 6, the gradient of the velocity potential, which denotes the velocity of the fluid, is given by

$$(\nabla\phi)^{(n)} = \sum_{i=1}^{N} \alpha_i^{(n)} \nabla p_i. \tag{8}$$

3.2 Time-marching scheme

At each time step, to solve the velocity potential for the entire domain, collocation is employed for boundary points. As mentioned above, conditions for collocation are given by the motion of the solid boundary and/or predicted from the free-surface boundary conditions, in which nonlinear terms are involved. By application of the second-order finite difference in time, the free-surface boundary conditions can be formulated as

$$\eta^{(n)} = \eta^{(n-2)} + 2\Delta t \left(\left.\frac{\partial\phi}{\partial z}\right|_{z=\eta} - \nabla_h\phi|_{z=\eta} \cdot \nabla_h\eta \right)^{(n-1)}, \tag{9}$$

$$\phi|_{z=\eta^{(n-1)}}^{(n)} = \phi|_{z=\eta^{(n-1)}}^{(n-2)} - 2\Delta t \left(g\eta + \frac{1}{2}\left(\nabla\phi \cdot \nabla\phi\right)|_{z=\eta} \right)^{(n-1)}. \tag{10}$$

In the above formulae, the required data on the right-hand side, including the nonlinear terms, are already known when solving the velocity potential in the entire domain at the n-th time step. General speaking, this explicit time-marching scheme can be regarded as a leap-frog approach, in which the velocity potential and the displacement at the free surface can be directly obtained from the above formulae, without any iteration. In the works of Wu et al. [27,28], the left-hand side in Eq. 10 was approximated as $\phi|_{z=\eta}^{(n)}$, while the first term on the right-hand side in Eq. 10 was estimated as $\phi|_{z=\eta}^{(n-2)}$. This might be fine for cases in which the nonlinearity is not strong. But since $\phi|_{z=\eta^{(n-1)}}^{(n)}$ is slightly different from $\phi|_{z=\eta}^{(n)}$, and $\phi|_{z=\eta^{(n-1)}}^{(n-2)}$ is also slightly different from $\phi|_{z=\eta}^{(n-2)}$, this minor difference in the approximations may cause significant errors in cases of strong nonlinearity.

Beneath the free surface, the no-flux boundary condition can be expressed as follows:

$$\sum_{i=1}^{N} \alpha_i^{(n)} \left(\nabla p_i \cdot \vec{n}\right)_{\vec{x}=\vec{x}_b}^{(n)} = \left(\vec{v}_b \cdot \vec{n}\right)_{\vec{x}=\vec{x}_b}^{(n)}. \tag{11}$$

3.3 Collocation for solving the velocity potential

The matrix formed by collocation of the boundary conditions can be expressed as

$$\begin{bmatrix} a_{1,1} & \cdots & a_{1,N} \\ & \ddots & \\ \vdots & a_{i,j} & \vdots \\ & \ddots & \\ a_{N,1} & \cdots & a_{N,N} \end{bmatrix}^{(n)} \begin{bmatrix} \alpha_1 \\ \vdots \\ \alpha_j \\ \vdots \\ \alpha_N \end{bmatrix}^{(n)} = \begin{bmatrix} b_1 \\ \vdots \\ b_i \\ \vdots \\ b_N \end{bmatrix}^{(n)} . \tag{12}$$

For boundary points near the free surface ($i = 1 \sim N_s$), the entries in the matrix in Eq. 12 are given as

$$a_{i,j}^{(n)} = p_j^{(n)}(\vec{x}_i), \quad b_i^{(n)} = \phi^{(n)}(\vec{x}_i), \tag{13a,b}$$

where $\phi^{(n)}(\vec{x}_i)$ is estimated by the free-surface boundary conditions. It should be noted that, regarding Eq. 10, the points for collocation are not on but near the free surface. These collocation points were on the free surface at the previous time step and might be above the free surface at the present time step. For boundary points on the body surface, $\vec{x}_i$ ($i = N_s + 1 \sim N$), the entries in the matrix are given as

$$a_{i,j}^{(n)} = \left(\nabla p_j \cdot \vec{n}\right)^{(n)}\Big|_{\vec{x}=\vec{x}_i}, \quad b_i^{(n)} = \left(\vec{v}_b \cdot \vec{n}\right)^{(n)}\Big|_{\vec{x}=\vec{x}_i}. \tag{14a,b}$$

3.4 Calculating the free-surface gradient

Apart from the above-mentioned descriptions, for solving the problem, the gradient of the free surface in Eq. 9 is also needed. Wang [14] developed an unstructured MEL model for the simulation of the nonlinear wave–body interaction with the desingularized boundary-integral-equation method. With a local interpolation method and high resolution of meshes, the free-surface intersection with the body can be precisely predicted. In the present study, the interpolating method of an RBF-type artificial neural network is adopted and the Gaussian function is chosen to be the RBF to fit the free surface. The collocation of fitting the free surface for three-dimensional wave problems in the present study is

$$\eta^{(n)}(x, y) = \sum_{i=1}^{N_S} \beta_i^{(n)} q_i(x, y), \quad q_i(x, y) = \exp\left(-\left(\frac{(x - x_i)^2 + (y - y_i)^2}{\sigma_i^2}\right)\right), \tag{15a,b}$$

where $q_i(x, y)$ is the two-dimensional RBF whose center is at (x_i, y_i) with $\beta_i^{(n)}$ as its weight factor. For the application of this approach to two-dimensional free-surface potential-flow problems one may refer to the work of Wu et al. [28]. The values of σ_i are the shape parameters denoting the range of influence of these RBFs. The reason for choosing the Gaussian RBF for fitting the free surface is that, when solving the weights of these RBFs, the matrix becomes sparse and almost banded and can be solved rapidly for small values of σ_i. However, as σ_i approaches zero, the Gaussian RBFs behave like delta functions and the value of η is always zero, except in the vicinities of these RBF centers. To avoid this kind of singular condition and to solve the problem rapidly, the value of σ_i should be chosen properly. Wu et al. [28] proposed that the value of the shape parameter of the Gaussian RBF should be greater than half of the nodal spacing to keep away from the singularity. According to our tests, this criterion would be fine if one's only concern were the accuracy of the calculated elevations of these free-surface nodes. However, for the accuracy of the elevation and the slope of the entire free surface, the shape parameter of the Gaussian RBF

should be greater than the nodal spacing. At each time step, when the free-surface displacement at n-th time step $\eta^{(n)}$ is known, the weights $\beta_i^{(n)}$ can be solved from the following linear algebraic system:

$$\begin{bmatrix} a_{1,1} & \cdots & a_{1,N_S} \\ & \ddots & \\ \vdots & a_{i,j} & \vdots \\ & \ddots & \\ a_{N_S,1} & \cdots & a_{N_S,N_S} \end{bmatrix}^{(n)} \begin{bmatrix} \beta_1 \\ \vdots \\ \beta_j \\ \vdots \\ \beta_{N_S} \end{bmatrix}^{(n)} = \begin{bmatrix} b_1 \\ \vdots \\ b_i \\ \vdots \\ b_{N_S} \end{bmatrix}^{(n)}, \tag{16}$$

where

$$a_{i,j}^{(n)} = q_j^{(n)}(x_i, y_i), \quad b_i^{(n)} = \eta^{(n)}(x_i, y_i). \tag{17a,b}$$

Once the $\beta_j^{(n)}$ have been solved, the gradient of the free surface can be obtained as

$$(\nabla_h \eta)^{(n)}(x, y) = \sum_{j=1}^{N_s} \beta_j^{(n)} \nabla_h q_j(x, y). \tag{18}$$

This equation is valid for the whole free surface in the computational domain, not only for these free-surface collocation nodes.

3.5 Procedures of numerical implementation

The marching procedures of the numerical implementation to find the physical unknowns at each new time step are listed as follows:

Procedure 1: The velocity potential ϕ in the entire domain and the particle displacement at the free surface η are given initially (at $n = -1$ and $n = 0$).

Procedure 2: The positions of the collocation points both on the body surface and close to the free surface for the n-th time step are updated. Also, the positions of the source points above the free surface and inside the body are updated.

Procedure 3: The velocity potential at the collocation points near the free surface is calculated by Eq. 10. Then, the condition for collocation near the free surface can be applied.

Procedure 4: After calculating the partial derivatives of the RBFs in Eq. 8 for all the collocation points, the solid-boundary condition beneath the free surface can then be applied by Eq. 11.

Procedure 5: The weights of the RBFs in Eq. 6, $\alpha_i^{(n)}$, are solved from the matrix collocated by procedures 3 and 4.

Procedure 6: The elevations of the boundary points on the free surface are calculated by Eq. 9. After solving the matrix formed by Eq. 15 (solving $\beta_i^{(n)}$), the free-surface gradients at these points are calculated by Eq. 18. It should be noted that these boundary points differ slightly from the collocation points.

Procedure 7: The velocity potential throughout the computational domain at the n-th time step can now be obtained from Eq. 6, and then the velocity in the entire domain can be calculated from Eq. 8.

Procedure 8: The number of time steps is checked. If the simulation has to be continued, procedure 2 for the next time step is then processed.

4 Model verifications

To study accuracy of the present model, the conservation of mass and energy for a problem of propagation of a solitary wave in a wave flume is chosen for verification. The still water depth and the wave height are 1.0 and 0.3 m,

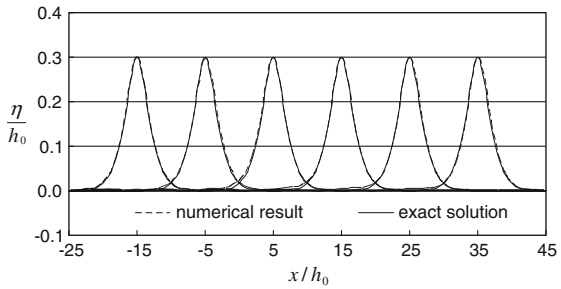

Fig. 1 The propagation of a solitary wave for the case $H/h_0 = 0.3$

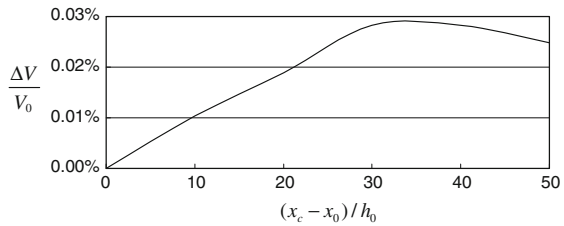

Fig. 2 The evolution of the relative mass error for the case of $H/h_0 = 0.3$

respectively. The horizontal range of the computation domain is chosen as $x = -25$ to 45 m and $y = -5$ to 5 m. The position of the wave crest (x_c) is initially at -15 m. The nodes on the free surface are arranged in equal spacing of $\Delta x = \Delta y = 1$ m, except those near the edge. The nodal spacing is about 1/12 of the wave length $L_{95\%}$, which is defined as the range of 95% of the mass of the solitary wave. The locations of the free-surface nodes near the edge are slightly shifted inward the domain to accelerate the computations, for arranging the free-surface nodes on the side wall spoils the matrix and consumes much computation time. The shifted distance is 1/4 of the nodal spacing. The same rule is followed for arranging boundary nodes at the bottom. For the two side walls, boundary nodes are arranged according to the same longitudinal nodal spacing as the free-surface and bottom nodes. To allow water-surface modulation, the nodes on the side walls in the vertical direction are purposely placed in the range from the bottom to an elevation higher than still water. This rule is followed for arranging boundary nodes on the walls at the two ends.

After some tests, it is found that the offset distance of sources from the boundary edge nodes should be greater than the usual 1.2 nodal spacing. Otherwise, some fluxes will flow across the side walls and the laws of physics will be violated. The same situation is also found for choosing the shape parameter of the Gaussian RBF when fitting the free surface. The shape parameter of the Gaussian RBF in the region should be greater than the nodal spacing, except those near the edges.

To obtain accurate computational results, there are three rows nearest to the edges chosen to enlarge the offset distance of the source points from the boundary and to enlarge the shape parameter of the Gaussian RBF for fitting the free surface. The offset distance is chosen as 1.5 nodal spacing while the shape parameter of the Gaussian RBF is chosen as 3 nodal spacings.

At each time step, after the elevation of the free-surface boundary nodes have been calculated, the entire free surface can be obtained by Eq. 15, including the elevation of each inter-surface line between the free surface and the side wall. The accuracy of the present model is verified by comparing the numerical results with those of the third-order solitary-wave solution of Grimshaw [29].

The propagation of the solitary wave along the centre line of the flume is illustrated in Fig. 1. From this figure, it is found that the elevation of the wave crest remains at 99.2% of the initial wave crest after the solitary wave has traveled a distance of 50 times the water depth. This implies that the energy is conserved. The total volume in the wave flume is calculated at each time step and conservation of fluid mass is also checked. The evolution of the relative mass error is shown as Fig. 2. From this figure, one can find that the total volume in the wave flume increases slightly as the solitary wave moves forward. The relative mass error remains within 0.03% during the simulation. Referring to the work of Ambrosi and Quartapelle [30], in which the problem was treated as one of Boussinesq type and solved by a finite-element method, the mass error of the present study is of the same order with their test of nodal spacing in $0.25\,h_0$. It should be noted that, with the present method, a coarser nodal spacing of $1.0h_0$ is sufficient to maintain the same order of mass errors. It should be pointed out that the wave height in the test for checking mass conservation in the work of Ambrosi and Quartapelle [30] was only 0.2, with a higher nonlinearity of the wave height, 0.3, being used in present study.

5 Model applications

5.1 Run-up of a solitary wave on a surface-piercing vertical cylinder

As an example of the applicability of the present model, the numerical simulation of the run-up of a solitary wave on a surface-piercing vertical cylinder is carried out. The horizontal range of the computation domain is $x = -25$ to 15 m and $y = -19.2$ to 19.2 m. The still-water depth and the incoming wave height are 1 and 0.3 m, respectively. The position of the wave crest (x_c) is initially at -15 m. A cylinder of radius 2 m is placed at $(0, 0)$. The rule for arranging the collocation points and source points described in the previous section is followed, but the nodal density is increased in the region of $x = -4$ to 4 m and $y = -4$ to 4 m with $\Delta x = \Delta y = 0.8$ m in response to the wave reflection from the cylinder. The propagation of the solitary is illustrated in Fig. 3. From this figure, one can see that water piles up on the impinged side as the solitary wave approaches the cylinder and reaches the highest value when the wave moves to $x_c = -2h_0$. The simulated run-up is $0.49h_0$, which is 4% higher than the result of $0.47h_0$ reported in the work of Ambrosi and Quartapelle [30]. After this stage, scattered waves begin to spread out. The higher run-up may be attributed to the new finite-difference approximation of the nonlinear free-surface boundary conditions.

5.2 Wave generation by a submerged moving object

5.2.1 Description of the problem

The wave problems studied in the previous section, with a fixed bottom at finite depth, can be simplified by a depth-integrated method to simpler problems, such as problems involving Boussinesq-type equations [30–34]. If monochromatic waves are of concern, these wave problems can be further simplified to mild-slope equations [35–38] by utilizing the periodicity of monochromatic waves. As a result of depth-integration, a three-dimensional problem reduces to a two-dimensional problem and a two-dimensional problem becomes a one-dimensional problem. Although some accuracy is lost, computation time is greatly reduced. Therefore, depth-integrated methods are widely applied for water-wave problems in ocean and coastal engineering.

Unlike depth-integrated methods, the present numerical method is applicable to nonlinear water-surface wave problems with infinite depth or with depth-varying bottom. Particularly, the present method is applicable to nonlinear wave-interaction problems with objects, fixed or moving, under water. To demonstrate the advantage of the present approach, problems of wave generation in infinite depth by a submerged moving object are chosen. The problem of wave generation by a submerged immobile spheroid in a steady stream of infinite depth, which is equivalent to the problem of wave generation in still water by a submerged moving spheroid with constant speed, has been investigated previously by others [39–46], and therefore provides a useful benchmark for the comparison of the present numerical results. As this case is a steady-state problem, while the present model is a time-domain numerical one, the submerged object must be accelerated from still condition to a specific speed and then travel beneath the free surface at this constant speed. The spheroid is considered moving in the x-direction at a speed of $V_b(t)$. A sieve technique [14] is applied to allow the body boundary to be still initially and accelerated to a speed of U_b gradually over a short period. The speed of the submerged spheroid as a function of time can be adjusted as

$$V_b(t) = U_b S_v(t), \tag{19}$$

where the sieve function $S_v(t)$ is chosen as the smooth function

$$S_v(t) = \begin{cases} 3(t/t_c)^2 - 2(t/t_c)^3, & \text{as } 0 \le t \le t_c \\ 1, & \text{as } t > t_c \end{cases} \tag{20}$$

and t_c is the end time of the sieve treatment, which, in this work, is set at $t_c = 0.3L/U_b$ where L is the length of the spheroid. The acceleration of the spheroid can be calculated by time derivation of the velocity function.

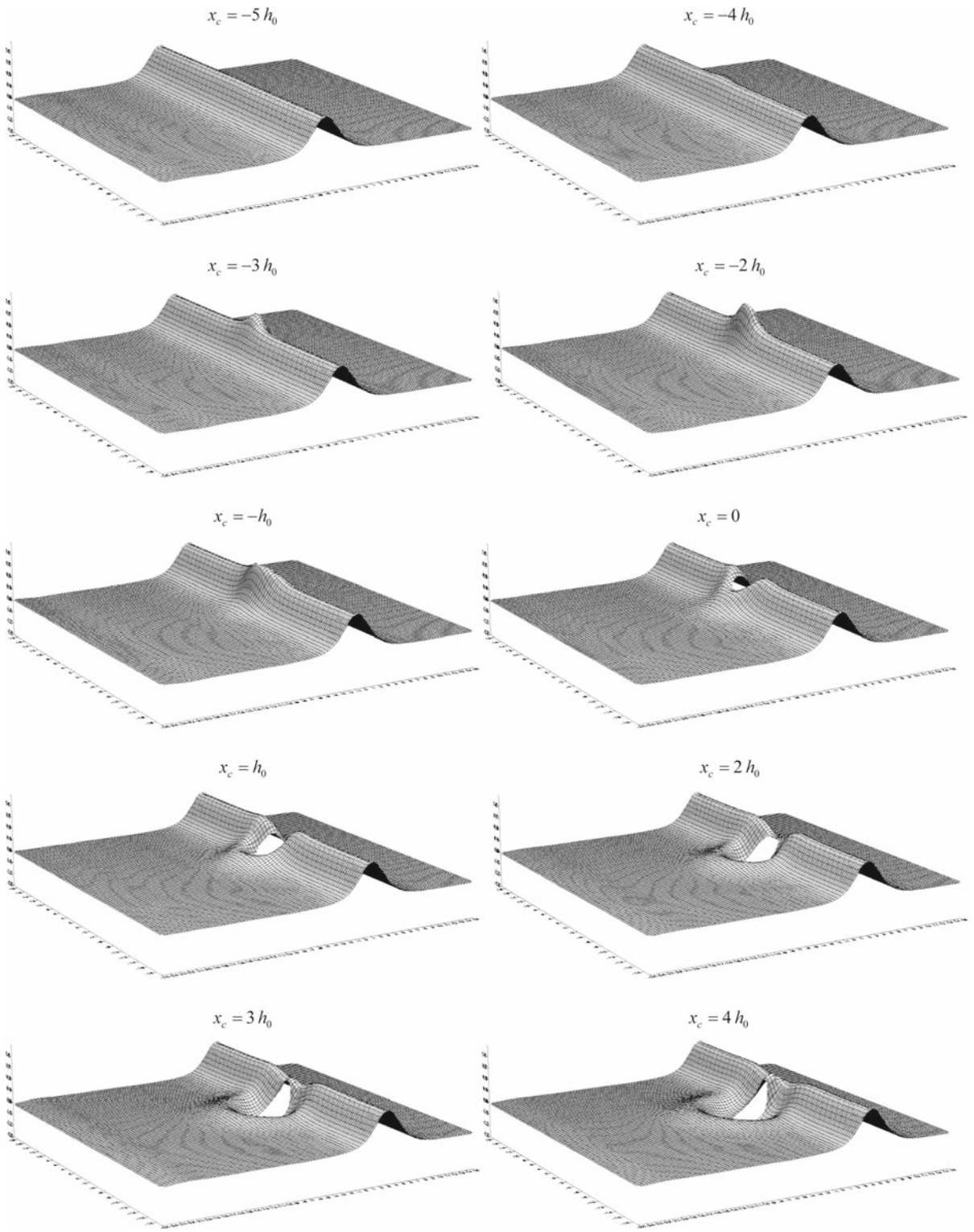

Fig. 3 The process of a solitary wave running up on a vertical cylinder in a three-dimensional view

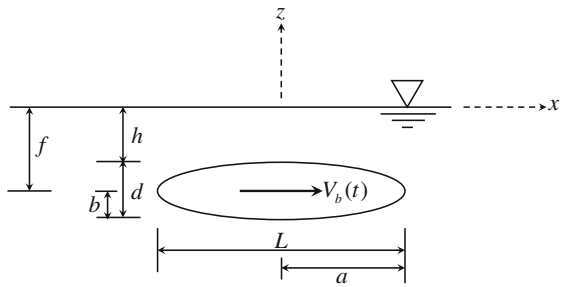

Fig. 4 Sketch of a spheroid and variables associated with its motion

5.2.2 Model setting

(a) Arrangements of boundary and source points

In the present study, the spheroid is set to travel at a submergence depth of f. The spheroid is set to be traveling with its center from $x = 0L$ to $x = 8L$ during the simulation. With a margin of $2L$ at the back of the spheroid and a margin of $1L$ in front, the range in the x-direction is $x = -2.5L$ to $9.5L$. For the angle of the wake a value of about 39° was mentioned in the above-listed papers, and also with a margin of $1L$, the range in the y-direction being $y = -4L$ to $4L$. The range in the horizontal lateral is far enough for the outgoing waves to travel before the spheroid reaches the terminal point in the computations. The body surface of the spheroid is defined as follows.

$$\frac{(x - x_c)^2}{a^2} + \frac{(y - y_c)^2 + (z - z_c)^2}{b^2} = 1, \tag{21}$$

where x_c, y_c and z_c are the coordinates of the moving spheroid center, and a and b are the semi-lengths of the major and minor axes ($a = L/2$ and $b = d/2$, where d is the diameter at the center of the spheroid). The sketch of the spheroid and the variables associated with the motion of the spheroid are given in Fig. 4. A schematic diagram showing the arrangement of the boundary and source points is shown in Fig. 5. From bow to stern, 16 longitudinal lines are set up on the body surface. Along each longitudinal line, the nodal spacing is properly chosen so that it nearly equals the nodal spacing in the lateral direction. It should be noted that the nodal spacing on the body surface is not constant and could be much smaller than that on the free surface.

(b) Spacing of free-surface nodes

For studying the required nodal resolution on the free surface, a spheroid with diameter-to-length ratio of 0.1 is chosen. The diameter-to-submergence ratio is 1.0. Thus, the water depth above the spheroid is half the diameter. The flow velocity is chosen for a Froude number of 0.5 ($F_L = U_b/\sqrt{gL}$). Simulations for various free-surface nodal spacings have been carried out. The range of the nodal spacing is from $L/14$ to $L/8$. Following the procedures described in the previous sections, the offset distance of the sources above the free surface is 1.2 nodal spacing and the shape parameter of the Gaussian RBF for fitting the free surface is equal to the nodal spacing. The arrangements on the body surface are kept the same in each run. Figure 6 shows the free-surface profiles of $y = 0$ at the stage $x_c = 2L$ for these tests. From the comparison in Fig. 6, one can observe that, when the free-surface nodal spacing is less than or equal to 1/12 spheroid length, it is sufficient to reveal the characteristics of the free-surface wave. From Fig. 6, one can also find that the distance between the first two peaks is about $1.3L$, which indicates there are about 16 nodes within one wave length.

Since present method is called "meshless", the boundary points on the free surface are unnecessarily arranged in a regular pattern of equal spacing. One can reduce the nodal density in some regions based on physical wave behaviors. It is anticipated that a wave decays when traveling away from the path of the spheroid. During the process of decaying, the waves become longer. Therefore, the nodal density in the regions away from the vicinity of the path of the spheroid can be reduced significantly. In the region of $|y| \geq 2L$, the nodal density is reduced by setting the nodal spacing to 1/6 spheroid length, while the nodal density is reduced by setting the nodal spacing to 1/8 and 1/10 spheroid length in the regions of $2L > |y| \geq L$ and $L > |y| \geq 0.5L$. Near the path of the spheroid, the nodal spacing is maintained at 1/12 spheroid length. A comparison of free-surface contours calculated by constant nodal

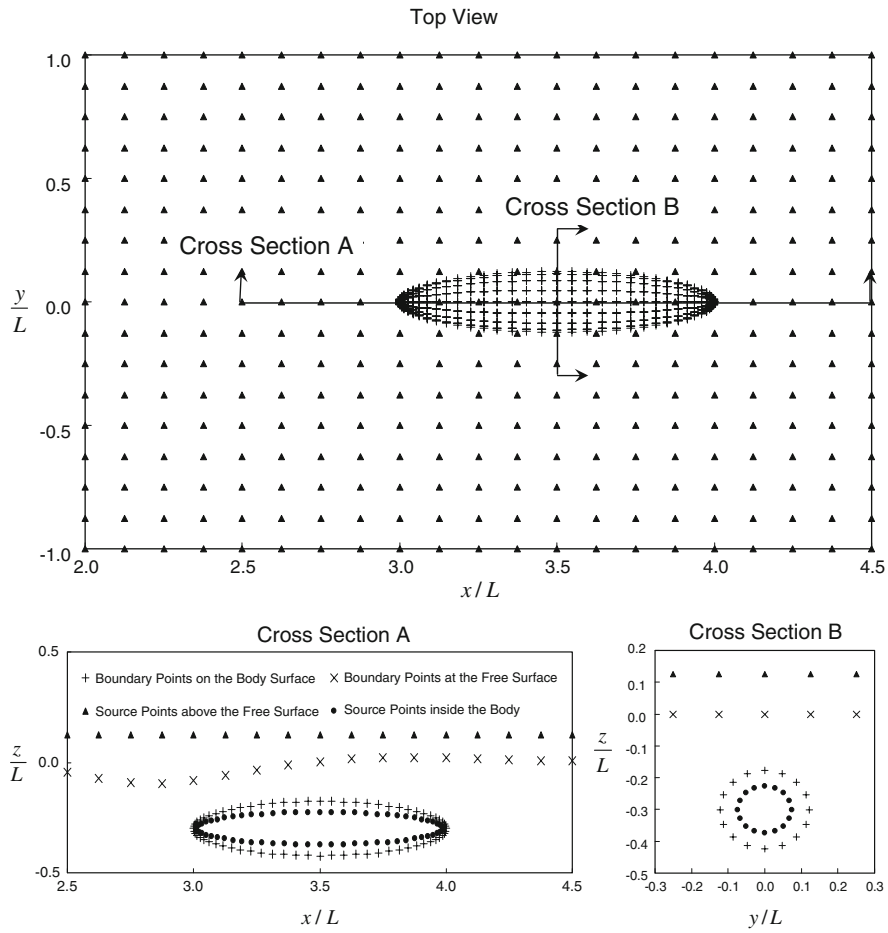

Fig. 5 Schematic diagram of boundary and source points arrangement

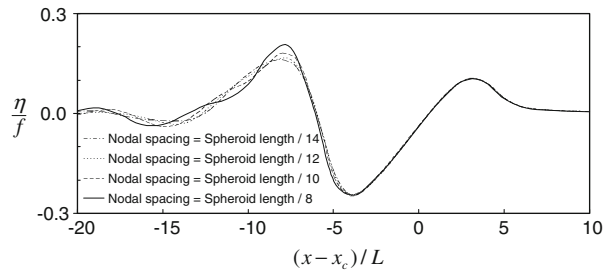

Fig. 6 Computed free-surface profiles of $y = 0$ at $x_c = 2L$ for testing the convergence of the free-surface nodal density (the spheroid for a diameter-to-length ratio 0.1 with a diameter-to-submergence ratio 1.0 and Froude number 0.5)

spacing with those contours calculated by varying nodal spacing at a stage of $x_c = 4L$ is shown in Fig. 7. From this figure, one can observe that the results calculated by both nodal arrangements nearly coincide.

5.2.3 Numerical results

Computed evolutions of both the free-surface elevation contours and the central free-surface profile for the case of a spheroid with a diameter-to-length ratio 0.1, with a diameter-to-submergence ratio 1.0 and Froude number 0.5 are shown in Figs. 8 and 9. The wave pattern in a three-dimensional view at the stage $x_c = 8L$ is shown in Fig. 10. It should be noted that the x- and z-axes in Fig. 9 are not drawn to scale.

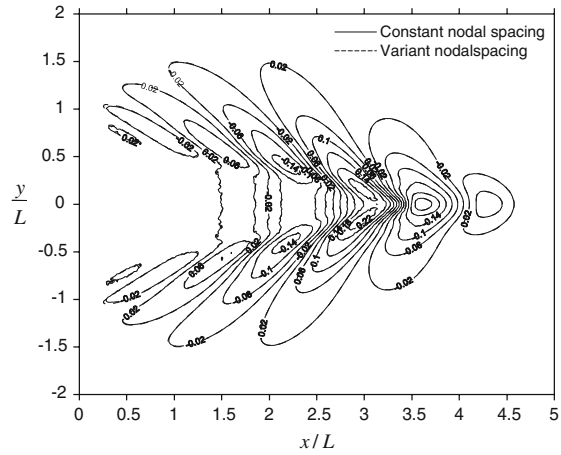

Fig. 7 Comparison of free-surface contours calculated in constant nodal spacing with those contours calculated in varying nodal spacing at $x_c = 6L$ (the spheroid in diameter-to-length ratio 0.1 with a diameter-to-submergence ratio 1.0 and Froude number 0.5)

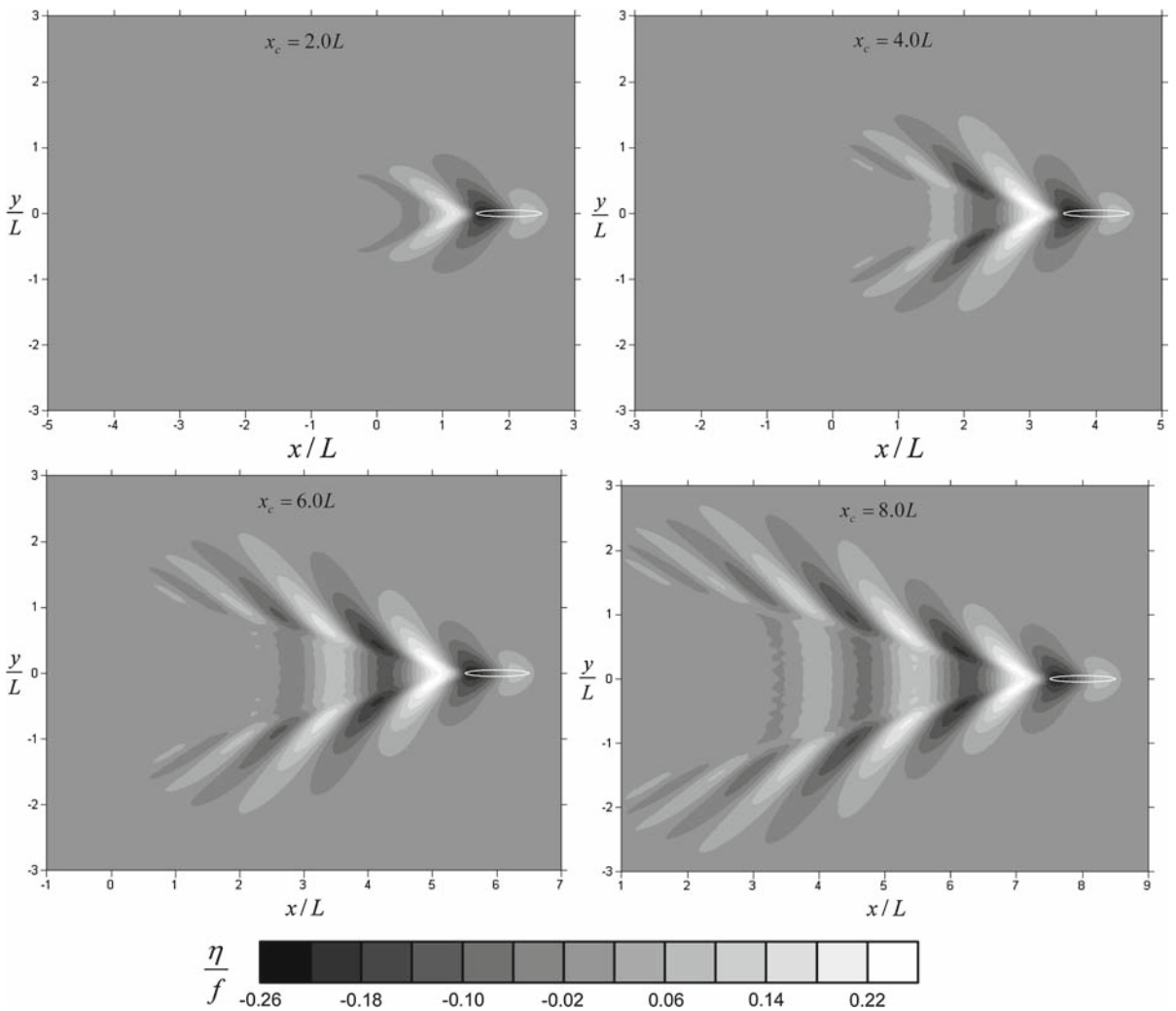

Fig. 8 Evolution of free-surface elevation contours for the case of a spheroid with a diameter-to-length ratio 0.1 with the diameter-to-submergence ratio 1.0 and Froude number 0.5

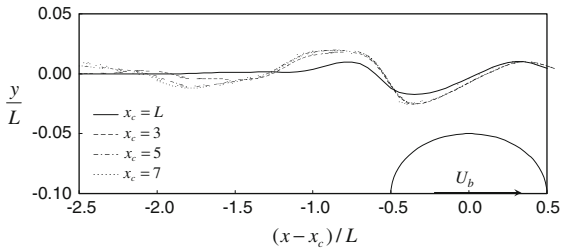

Fig. 9 Evolution of the central free-surface profile for the case of a spheroid with a diameter-to-length ratio 0.1 with the diameter-to-submergence ratio 1.0 and Froude number 0.5

From Fig. 9 one can see that, when the spheroid has traveled for one hull length ($x_c = L$), the free-surface humps up above the first half of the hull and sinks down to the lowest just right at the stern. As the spheroid moves further forward for about two more hull lengths ($x_c = 3L$), the hollow becomes more pronounced and another hump arises behind the hollow while the first hump keeps its shape and the generated waves spread out to both sides. As the spheroid moves further, the wave shape in the vicinity of the spheroid approaches the steady state gradually and the generated waves keep on spreading out. From the evolution of the free-surface wave, it may be concluded that the wave pattern within the range of $3L$ from the center of the spheroid achieves the steady state approximately after the stage at $x_c = 8L$.

Surface elevations at the centerline computed from other models, as a benchmark for comparison of the present numerical results, are digitized from the work of Tuck and Scullen [45], in which the fully nonlinear model of Scullen [44] was used to test the significance of nonlinearity. The nonlinear terms were optional in the code of Scullen [44]. A comparison of the computed central free-surface profile at steady state with those reported in the work of Tuck and Scullen [45] is shown in Fig. 11. It should be noted that the results of Tuck and Scullen [45], for a spheroid resting firmly in a steady current flowing forward in the positive x-direction and a central free-surface profile, was shown on a dimensionless scale of k_0x and k_0z, where $k_0 = g/U_b^2$; these have been converted for comparison with the present results, on a dimensionless scale of $(x - x_c)/L$ and η/f. Comparing with the other three linear results, one can observe better agreement between the present result and the result of the nonlinear model, which was dubbed the Neumann–Stokes model in the paper of Tuck and Scullen [45].

For further comparisons, a spheroid with a diameter-to-length ratio of 0.245 is chosen. The diameter-to-submergence ratio is 0.816. Numerical computations with the Froude number ranging from 0.4 to 0.8 have been carried out. The range of the computational domain is the same as that in previous simulations, while the spheroid is more voluminons. Figure 12 shows the wave patterns with a clear wake transition at $x_c = 8L$ for various Froude numbers. For low Froude number (for example F_L =0.4), the dominant waves are of a transverse form, while, as the Froude number gets higher, the transverse waves lengthen and divergent waves become more apparent. It is of interests to

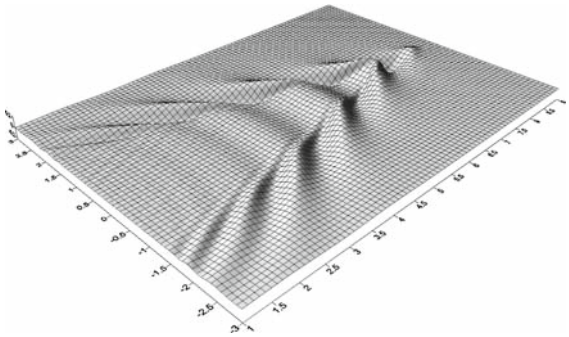

Fig. 10 Wave pattern in a three-dimensional view at $x_c = 8L$ for the case of a spheroid with a diameter-to-length ratio 0.1, with the diameter-to-submergence ratio 1.0 and Froude number 0.5

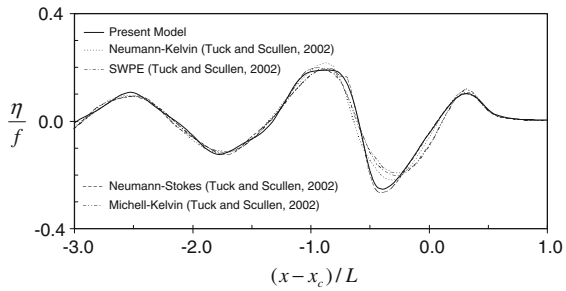

Fig. 11 Computed central free-surface profile at steady state compared with other numerical results, for the case of a spheroid with a diameter-to-length ratio 0.1, with the diameter-to-submergence ratio 1.0 and Froude number 0.5

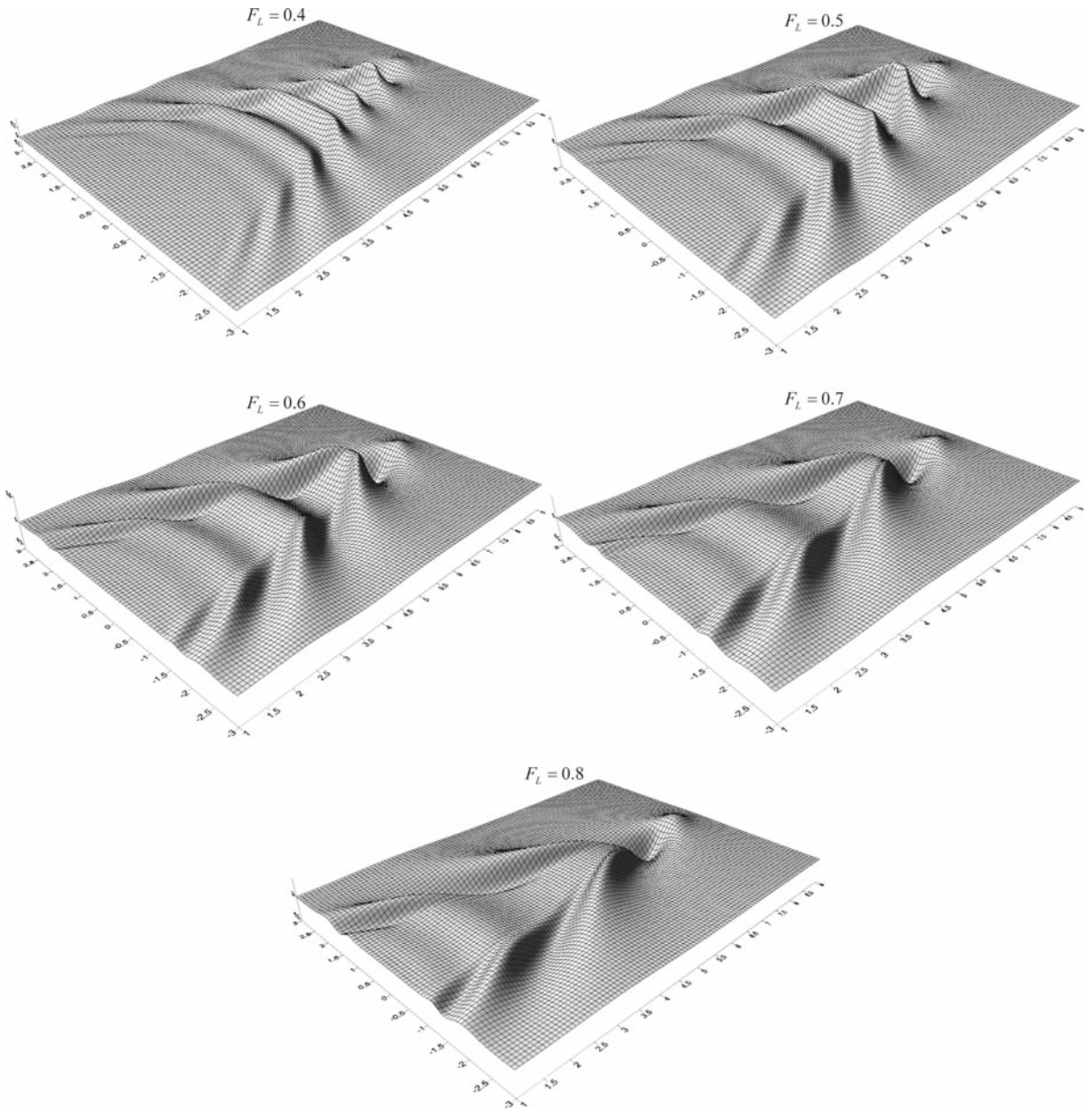

Fig. 12 Wave patterns in a three-dimensional view at $x_c = 8L$ for the case of a spheroid with a diameter-to-length ratio 0.245 and with diameter-to-submergence ratio 0.816

note that the pattern of the transverse waves of F_L =0.5 in Fig. 12 is similar to the pattern of the transverse waves in Fig. 10, for the two spheroids are traveling at the same speed. However, in Fig. 10 the divergent waves are more pronounced due to the shallower submergence but the free-surface deviation is smaller because of the slenderness of the spheroid.

When the steady state of the flow in the vicinity of the spheroid is achieved, the resistance force acting on the body can be calculated by the following integral:

$$R = \rho \int_{\partial B} \frac{1}{2} n_x \left|\vec{u}\right|^2 \mathrm{d}S, \tag{22}$$

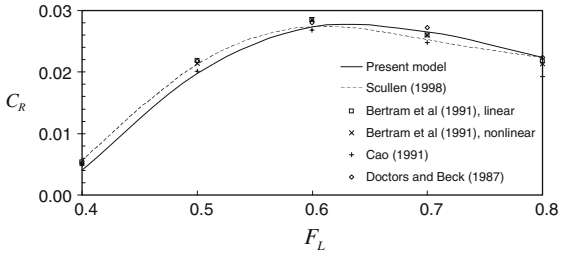

Fig. 13 Comparison of resistance coefficient computed by the present model with other numerical results, for the case of a spheroid with a diameter-to-length ratio 0.245 and with diameter-to-submergence ratio 0.816

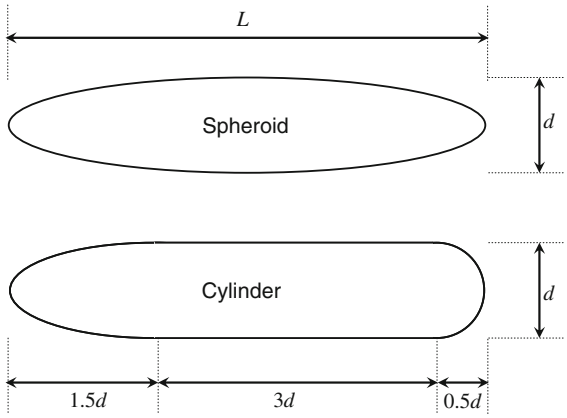

Fig. 14 Bodies considered in the wave-resistance problem in [13]

where ρ denotes the density of the fluid, ∂B denotes the body surface, and $\vec{u}$ is the relative velocity with respect to the moving spheroid. Therefore $\vec{u} = \vec{v} - U_b \vec{i}$. To compare the present results with those of other works, the wave-resistance coefficient is used. It is defined as

$$C_R = \frac{R}{\frac{\pi}{6}\rho g L d^2}. \tag{23}$$

Figure 13 shows the results of the present method in comparison with those reported by Scullen [44] which included results produced by others [41–43]. All the data for comparison were digitized from the work of Scullen [44]. The numerical methods employed by Doctors and Beck [41] and Cao [43], as well as the present one, were time-dependent formulations. The steady states were extrapolated to estimate the approximation. Numerical results of all six methods are in good agreement with one another. From Fig. 13, one can find that the drag-force coefficient appears to have the largest value at $F_L = 0.6$.

5.2.4 Wave pattern generated by objects of different shapes

For investigating the effects on the accuracy of the desingularized distance of the desingularized boundary-integral method in free-surface flow problems, Lalli [13] carried out several test cases, including wave patterns generated by the steady motion of two different submerged bodies. One of these two submerged bodies was a spheroid of length-to-diameter ratio 0.2, while the other one is a streamlined circular cylinder with a half-sphere-shaped "bow" and the "stern" composed of a half-spheroid. The length of the half-spheroid was $1.5d$. The appearances of these two bodies are shown in Fig. 14. The submergence-to-diameter ratio was 1.0. Thus, the water depth above the body was $0.5d$. The Froude number for the spheroid case and the cylinder case are 0.447 and 0.448, respectively. Lalli's results [13] were compared with their own experimental data.

The range of the computational domain for simulating is the same as in previous cases. The arrangements of the free-surface collocation points and sources above the free surface are also the same. The collocation points on the body surface and sources inside the body follow the same arrangement as in pervious cases. Wave patterns in a three-dimensional view at $x_c = 8L$ for these two cases are shown in Fig. 15. These two patterns are very similar, but different at two dominant peaks above and at the back of the body. For a streamlined cylinder, the first peak above the body is higher, while the second peak is lower and wider. The present model is verified by comparing the free-surface profiles at $y = 2.3L$, $2.8L$, and $4.4L$ with numerical results and experimental data reported in [13], from which data for comparison have been digitized. Comparison of the present results with experimental data and

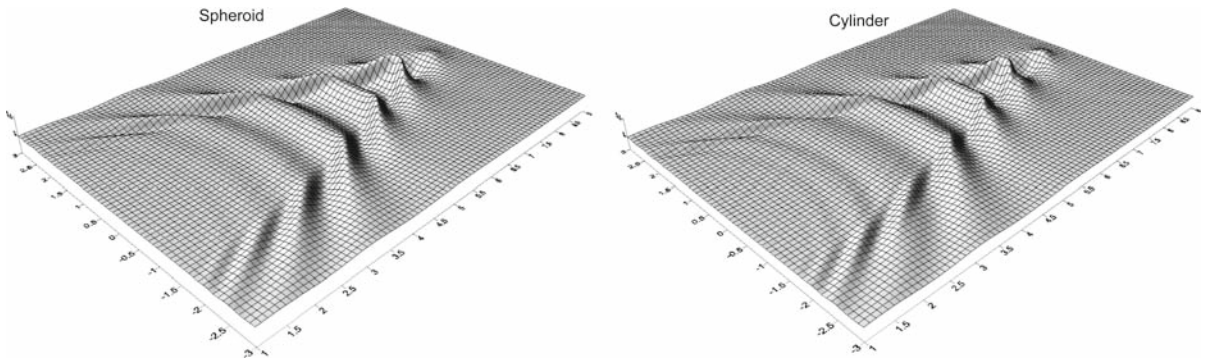

Fig. 15 Wave patterns in a three-dimensional view at $x_c = 8L$ for both bodies for cases of diameter-to-length ratio 0.2, diameter-to-submergence ratio 1.0 and Froude number 0.447 and 0.448, respectively

the numerical results of Lalli [13] are shown in Figs. 16 and 17. A better agreement of the present results with the experimental data can be found.

6 Conclusions

Following the approach of Wu et al. [28], which is a boundary-type meshless method with non-iterative leap-frog time-marching scheme, and applying a more accurate finite-difference approximation in the time domain to the free-surface boundary condition, a numerical model to simulate three-dimensional fully nonlinear water-surface

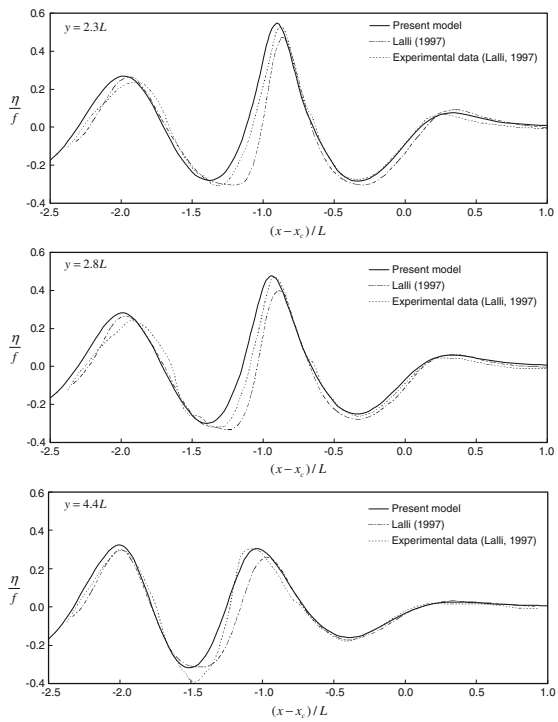

Fig. 16 Comparison of the present results with experimental data and the numerical results of Lalli [13] for a spheroid with a diameter-to-length 0.2, diameter to submergence ratio 1.0 and Froude number 0.447

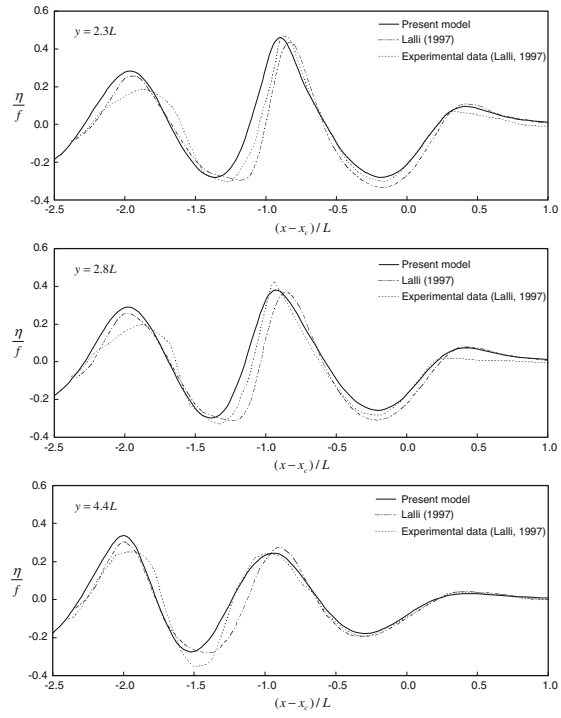

Fig. 17 Comparison of the present results with experimental data and the numerical results of Lalli [13] for the case of a streamlined cylinder with a diameter-to-length 0.2, diameter-to-submergence ratio 1.0, and Froude number 0.448

wave problems has been developed. The time-marching scheme formulated here is an explicit one that does not require iteration when evaluating the velocity potential and the displacement at the free surface for forward time steps. Choosing the fundamental solution of the Laplace operator as the solution form of the velocity potential and placing all the singularities outside the computational domain, only collocation points along the boundary are needed for solving wave problems. Thus, neither element in the domain nor meshes on the boundary are required. The task of mesh generation is omitted. According to tests described in Sects. 3 and 4, less resolution of nodes is needed for revealing the characteristic of the nonlinear waves, thus computer memory is saved.

The idea of MFS is similar to the indirect DBIE, while the difference is that DBIE still needs some numerical integration along the surface on the boundary or outside the domain, but MFS only employs collocation about the boundary points without needing any mesh generation and numerical integration.

The accuracy of the present model is verified first by comparing mass and energy conservation and surface profile of a propagating solitary wave with an exact solution [29]. It may be attributed to the present new formulation of the nonlinear free-surface boundary conditions that the numerical result of solitary wave run-up on a vertical cylinder reaches $0.49h_0$, which is slightly higher than the result found by Ambrosi and Quatapelle [30]. The usefulness of the present model is further confirmed by employing it to simulate wave generation in infinite water depth by a submerged moving object. From comparisons of the present results with other numerical results [13,41–45] and experimental data [13], very good agreement is observed.

References

1. Longuet-Higgins HS, Cokelet ED (1976) The deformation of steep waves on water, I, a numerical method of computation. Proc R Soc Lond A350:1–26. doi:10.1098/rspa.1976.0092
2. Issacson M (1982) Nonlinear wave effects on fixed and floating bodies. J Fluid Mech 120:267–281. doi:10.1017/S0022112082002766
3. Dommermuth DG, Yue DKP (1987) Numerical simulations of nonlinear axisymmetric flows with a free surface. J Fluid Mech 178:195–219. doi:10.1017/S0022112087001186
4. Grilli ST, Skourup J, Svendsen IA (1989) An efficient boundary element method for nonlinear water waves. Eng Anal Bound Elem 6:97–107. doi:10.1016/0955-7997(89)90005-2
5. Cooker MJ, Peregrine DH, Skovggard O (1990) The interaction between a solitary wave and a submerged semicircular cylinder. J Fluid Mech 215:1–22. doi:10.1017/S002211209000252X
6. Ohyama T, Nadaoka K (1991) Development of a numerical wave tank for analysis of nonlinear and irregular wave field. Fluid Dyn Res 8:231–251. doi:10.1016/0169-5983(91)90045-K
7. Grilli ST, Guyenne P, Dias F (2001) A fully nonlinear model for three-dimensional overturning waves over an arbitrary bottom. Int J Numer Methods Fluids 35:829–867. doi:10.1002/1097-0363(20010415)35:7<829::AID-FLD115>3.0.CO;2-2
8. Tsai WT, Yue DKP (1996) Computation of nonlinear free-surface flows. Annu Rev Fluid Mech 28: 249–278
9. Rokhlin V (1985) Rapid solution of integral equations of classical potential theory. J Comput Phys 60:187–207. doi:10.1016/0021-9991(85)90002-6
10. Hackbusch W, Nowak ZP (1989) On the fast matrix multiplication in the boundary element method by panel clustering. Numer Math 54:463–491. doi:10.1007/BF01396324
11. Beylkin G, Coifman R, Rokhlin V (1991) Fast wavelet transforms and numerical algorithms I. Commun Pure Appl Math 44: 141–183. doi:10.1002/cpa.3160440202
12. Cao YS, Schultz WW, Beck RF (1991) 3-dimensional desingularized boundary integral methods for potential problems. Int J Numer Methods Fluids 12:785–803. doi:10.1002/fld.1650120807
13. Lalli F (1997) On the accuracy of the desingularized boundary integral method in free surface flow problems. Int J Numer Methods Fluids 25:1163–1184. doi:10.1002/(SICI)1097-0363(19971130)25:10<1163::AID-FLD614>3.0.CO;2-5
14. Wang QX (2005) Unstructured MEL modeling of nonlinear unsteady ship waves. J Comput Phys 210:368–385. doi:10.1016/j.jcp.2005.04.012
15. Hardy RL (1971) Multiquadric equations of topography and other irregular surfaces. J Geophys Res 76:1905–1915. doi:10.1029/JB076i008p01905
16. Franke C (1982) Scattered data interpolation: test of some methods. Math Comput 38:181–200. doi:10.2307/2007474
17. Moody J, Darken C (1989) Fast-learning in networks of local tuned processing units. Neural Comput 1:281–294. doi:10.1162/neco.1989.1.2.281
18. Kansa JE (1990) Multiquadrics—a scattered data approximation scheme with applications to computational fluid dynamics—II, Solutions to parabolic, hyperbolic and elliptic partial differential equations. Comput Math Appl 19:127–145. doi:10.1016/0898-1221(90)90270-T

19. Du CJ (1999) Finite-point simulation of steady shallow water flows. J Hydraul Eng 125:621–630. doi:10.1061/(ASCE)0733-9429(1999)125:6(621)
20. Du CJ (2000) An element-free Galerkin method for simulation of stationary two-dimensional shallow water flows in rivers. Comput Methods Appl Mech Eng 182:89–107. doi:10.1016/S0045-7825(99)00087-0
21. Zhou X, Hon YC, Cheung KF (2004) A grid-free, nonlinear shallow-water model with moving boundary. Eng Anal Bound Elem 28:967–973. doi:10.1016/S0955-7997(03)00124-3
22. Young DL, Jane SJ, Lin CY, Chiu CL, Chen KC (2004) Solution of 2D and 3D Stokes law using multiquadratics method. Eng Anal Bound Elem 28:1233–1243. doi:10.1016/j.enganabound.2003.04.002
23. Ata R, Soulaimani A (2005) A stabilized SPH method for inviscid shallow water flows. Int J Numer Methods Fluids 47:139–159. doi:10.1002/fld.801
24. Ma Q (2005) Meshless local Petrov–Galerkin method for two-dimensional nonlinear water wave problems. J Comput Phys 205:611–625. doi:10.1016/j.jcp.2004.11.010
25. Golberg MA, Chen CS (1998) The method of fundamental solutions for potential, Helmholtz and diffusion problems. In: Golberg MA (ed) Boundary integral methods-numerical and mathematical aspects. Computational Mechanics Publications, pp.103–176
26. Young DL, Chen KH, Lee CW (2005) Novel meshless method for solving the potential problems with arbitrary domain. J Comput Phys 209:290–321. doi:10.1016/j.jcp.2005.03.007
27. Wu NJ, Tsay TK, Young DL (2006) Meshless simulation for fully nonlinear water waves. Int J Numer Methods Fluids 50:219–234. doi:10.1002/fld.1051
28. Wu NJ, Tsay TK, Young DL (2008) Computation of nonlinear free-surface flows by a meshless numerical method. J Waterw Port Coast Ocean Eng 134:97–103. doi:10.1061/(ASCE)0733-950X(2008)134:2(97)
29. Grimshaw R (1971) The solitary wave in water of variable depth, part 2. J Fluid Mech 9:611–622. doi:10.1017/S0022112071000739
30. Ambrosi D, Quartapelle L (1998) A Taylor–Galerkin method for simulation nonlinear dispersive waves. J Comput Phys 146:546–569. doi:10.1006/jcph.1998.6027
31. Peregrine DH (1967) Long waves on beach. J Fluid Mech 27:815–827. doi:10.1017/S0022112067002605
32. Nwogu O (1993) An alternative form of Boussinesq equations for near shore wave propagation. J Waterw Port Coast Ocean Eng 119:618–638. doi:10.1061/(ASCE)0733-950X(1993)119:6(618)
33. Wei G, Kirby JT, Grilli ST, Subramanya R (1995) Time-dependent numerical code for extended Boussinesq equations. J Fluid Mech 294:71–92. doi:10.1017/S0022112095002813
34. Gobbi MF, Kirby JT (1999) Wave evolution over submerged sills: tests of a high order Boussinesq model. Coast Eng 37:57–96. doi:10.1016/S0378-3839(99)00015-0
35. Berkhoff JCW (1972) Computation of combined refraction–diffraction. In: Proc. 13th conf. eng., ASCE, Vancouver; pp. 471–490
36. Liu PLF, Tasy TK (1984) Refraction–diffraction model for weakly nonlinear water waves. J Fluid Mech 136: 453–466
37. Tang Y, Ouellet Y (1996) A new kind of nonlinear mild-slope equation for combined refraction–diffraction of multi-frequency waves. J Coast Eng 31:3–36. doi:10.1016/S0378-3839(96)00050-6
38. Chen MY, Mei CC (2006) Second-order refraction and diffraction of surface water waves. J Fluid Mech 552:137–166. doi:10.1017/S0022112005008530
39. Havelock TH (1931) The wave resistance of a spheroid. Proc R Soc Lond, A131:275–285. doi:10.1098/rspa.1931.0052
40. Farell C (1973) On the wave resistance of a submerged spheroid. J Ship Res 17:1–11
41. Doctors LJ, Beck RF (1987) Convergence properties of the Neumann–Kelvin problem for a submerged body. J Ship Res 31:227–234
42. Bertram V, Schultz WW, Cao Y, Beck RF (1991) Nonlinear computations for wave drag, lift and moment of a submerged spheroid. Ship Technol Res 38:3–5
43. Cao Y (1991) Computations of nonlinear gravity waves by a desingularised boundary integral method. Ph.D. dissertation, Department of Naval Architecture and Marine Engineering, The University of Michigan
44. Scullen DC (1998) Accurate computation of steady nonlinear free-surface flows. Ph.D. dissertation, Department of Applied Mathematics, The University of Adelaide
45. Tuck EO, Scullen DC (2002) A comparison of linear and nonlinear computations of waves made by slender submerged bodies. J Eng Math 42:255–264. doi:10.1023/A:1016131128042
46. Kent CP, Choi W (2007) An explicit formulation for the evolution of nonlinear surface waves interacting with a submerged body. Int J Numer Methods Fluids 55:1019–1038. doi:10.1002/fld.1504